Article

A Ratiometric Biosensor for Aggregation-Induced Emission-Guided Precise Photodynamic Therapy

Kai Han, Shi-Bo Wang, Qi Lei, Jing-Yi Zhu, and Xian-Zheng Zhang

ACS Nano, **Just Accepted Manuscript** • DOI: 10.1021/acsnano.5b04243 • Publication Date (Web): 08 Sep 2015

A Ratiometric Biosensor for Aggregation-Induced Emission-Guided Precise Photodynamic Therapy

*Kai Han [1,†], Shi-Bo Wang [1,2,†], Qi Lei [1], Jing-Yi Zhu [1], Xian-Zheng Zhang [1,2,]**

[1] Key Laboratory of Biomedical Polymers of Ministry of Education & Department of Chemistry, Wuhan University, Wuhan 430072, China, [2] The Institute for Advanced Studies, Wuhan University, Wuhan 430072, China.

ABSTRACT: Photodynamic therapy faces the barrier in choosing the appropriate irradiation region and time. In this paper, a matrix metalloproteinase-2 (MMP-2) responsive ratiometric biosensor was designed and synthesized for aggregation-induced emission (AIE)-guided precise photodynamic therapy. It was found that the biosensor presented the MMP-2 responsive AIE behavior. Most importantly, it could accurately differentiate the tumor cells from the healthy cells by the fluorescence ratio between freed tetraphenylethylene (TPE) and protoporphyrin IX (PpIX, internal reference). *In vivo* study demonstrated that the biosensor could preferentially accumulate in the tumor tissue with a relative long blood retention time. Note that the intrinsic fluorescence of PpIX and MMP-2-triggered AIE fluorescence provided a real-time feedback which guided precise photodynamic therapy *in vivo* efficiently. This strategy demonstrated here opens a window in the precise medicine, especially for phototherapy.

KEYWORDS: photodynamic therapy · ratiometric biosensor · MMP-2 responsive · aggregation-induced emission · tumor

Photodynamic therapy (PDT) has obtained increased attention during the last decades, mostly because of the non-invasiveness to normal tissues as well as great potential in highly accurate tumor therapy.[1-3] Although various photodynamic therapy systems have been developed for tumor therapy, the conventional photodynamic therapy systems still confront the challenge of tumor recognition. Since the photodynamic antitumor effect of photosensitizer is mainly motivated by the formation of reactive oxygen species (ROS) under light irradiation.[4,5] However, the fluorescence of photosensitizer is always "on", leading to the constant intensity as well as abundant nonspecific signal.[6,7] Consequently, discernment of healthy cells from diseased ones became extremely difficult. Thus, choosing an appropriate irradiation region and time is highly desirable for photodynamic therapy with reduced side effects.

Recently, a new concept of "stimuli-triggered imaging" guided therapy was proposed to realize the visible and precise phototherapy.[8,9] This strategy mainly utilizes the specific tumor microenvironments such as acidosis, hypoxia and overexpressed enzyme to activate the fluorescence signal change, which can guide the phototherapy.[10] However, fluorescence imaging whose response to the tumor microenvironment is basically limited to the change of fluorescence emission intensity. And fluorescence intensity is severely affected by the local content of biosensor in tumor region as well as microenvironments.[11] As a result, the background fluorescence is always mistaken for weak fluorescence, this false positive fluorescence will cause unwanted side effects.[12] To overcome these dilemmas, ratiometric fluorescence imaging

technique has been developed to measure the fluorescence intensity ratio at two different wavelengths, which provides a built-in self-correction regardless of the local biosensor concentration and environmental affects.[13-15] However, very few works have been done in ratiometric sensor guided therapy,[16] and the imaging and therapy procedures were generally implemented separately. In addition, construction of ratiometric sensors is always based on the principle of structure changing-induced wavelength shift. All these issues make the fabrication of these nanodevices complicated and costly.[17]

Here, *for the first time*, we reported a ratiometric fluorescence biosensor for matrix metalloproteinase-2 (MMP-2) responsive aggregation-induced emission (AIE)-imaging guided photodynamic therapy (Scheme 1). Compared with other tumor microenvironments that are confused easily by some specific biological environments, for example, acidity also happened in inflammation region, the overexpression of MMP-2 is a striking feature for many types of solid tumors.[18] In this report, the biosensor consisted of a photosensitizer protoporphyrin IX (PpIX) and an AIE molecular tetraphenylethylene (TPE)[19-21] using PEGylated Pro-Leu-Gly-Val-Arg (PLGVR) peptide sequence as a linker. The biosensor thus obtained was designated as TPPP (TPE-PLGVR$_2$-(PEG$_8$)$_2$-K(PpIX)). PpIX was employed as both the photosensitizer and fluorescence internal reference. When TPPP arrived at the tumor tissue, the overexpressed MMP-2 in tumor region hydrolyzed the PLGVR sequence, leading to the detachment of TPE and PEGylated PpIX. The ratiometric fluorescence ratio between TPE and PpIX could evaluate the MMP-2 expression level. On the other hand, this aggregation-induced emission provided a visible and accurate feedback of the photodynamic time and region. The *in vivo* antitumor effect using a nude mice model was further investigated.

RESULTS AND DISCUSSION

Synthesis and Characterization of Biosensor. Standard fluorenylmethyloxycarbonyl solid phase peptide synthesis method was used to obtain TPPP.[22] The synthesis of TPPP was performed in Figure S1 and the validity of TPE-COOH was confirmed in Figure S2. The theoretical molecular weight of TPPP was 2602, while the multi-charge peak was found at 1302.98 ($[M+2H]^{2+}$) in electrospray ionization-mass spectrum (ESI-MS, Figure S3A). Although both TPE and PpIX were extremely hydrophobic, TPPP showed well water-solubility due to the introduction of hydrophilic PEG segment. Transmission electron microscope image (TEM) revealed that amphiphilic TPPP could self-assemble to form spherical nanoparticles in PBS buffer with the size distribution of 27.9 ± 7.3 nm (Figure 1A). This self-assembly behavior in aqueous solution was due to the fact that TPE and PpIX formed the core owing to the hydrophobic interaction, while PEG segment formed the hydrophilic shell. Besides, negligible size change of nanoparticles was observed when TPPP was incubated with diluted DMEM medium containing FBS (fetal bovine serum) (Figure S4A), suggesting these nanoparticles would not disassemble or aggregate in the presence of serum proteins. All these issues ensured that the sub-100 nm nanoparticles could preferentially accumulate in tumor tissue due to the enhanced permeability and retention (EPR) effect.[23] The improved water-solubility was further verified by the UV-vis spectrum (Figure 1B). Unlike the free PpIX which presented greatly broadened split Soret band (maxima at 352 and 450 nm), a Soret band at around 400 nm was observed in TPPP due to the negligible π-π stacking.[24]

The improved water-solubility of TPPP also accelerated the formation of singlet oxygen ($^1O_2$) under light irradiation. 2′,7′-dichlorofluorescin diacetate (DCFH-DA) was chosen as the sensor, since the non-fluorescent dye DCFH-DA can be rapidly oxidized to 2′,7′-dichlorofluorescin (DCF) with green fluorescence.[25] The fluorescence spectra results showed the fluorescence

increment of DCF in TPPP group was significantly higher than that in PpIX group due to the fact that improved solubility of photosensitizer decreased the aggregation-induced self-quenching behavior (Figure 1C). As a control, undetectable change was observed in water group. To verify that the enhanced formation $^1O_2$ was related to improved water-solubility of photosensitizer, $(PEG_8)_2$-PpIX was incubated with DCFH-DA. As expected, the fluorescence increment in $(PEG_8)_2$-PpIX group was also significantly higher than that in PpIX group (Figure S4B). Besides, Similar results were also found in intracellular ROS generation. None green fluorescence or limited green fluorescence was found in blank SCC-7 (squamous cell carcinoma) cells (Figure 1D), TPE-treated (Figure 1E) and PpIX-treated SCC-7 cells (Figure 1F), respectively. In a sharp contrast, significantly brighter green fluorescence was observed in TPPP group (Figure 1G). Quantitative result of fluorescent intensity revealed that the fluorescence in TPPP group was nearly twofold to that in PpIX group (Figure S5). All these results indicated the good ROS generation ability of TPPP.

MMP-2 Detection by Fluorescence Spectra. Since TPE was conjugated to PEGylated PpIX with a MMP-2 hydrolyzable substrate PLGVR peptide sequence, it was expected to show MMP-2-responsive AIE. The fluorescence spectra was measured when TPPP was incubated with MMP-2. As shown in Figure 2A, the fluorescence of TPE increased very rapidly with time prolonging when TPPP (80 mg/L) was incubated with 0.4 mg/L MMP-2. Considering that the fluorescence of TPE was unchangeable with time prolonging in the absence of MMP-2 (Figure S6A), the rapid fluorescence increase of TPE was attributed to the fact that hydrolysis of PLGVR by MMP-2 liberated TPE molecule, the enhanced hydrophobicity severely restricted the free rotation of phenyl group, resulting in aggregation-induced emission.[26] Besides, fluorescence

intensity increased more quickly with increasing concentration of MMP-2 (Figure 2B), indicating that the hydrolysis rate of PLGVR sequence was MMP-2 concentration-dependent.

Furthermore, the fluorescence ratio between TPE and PpIX (F_{TPE}/F_{PpIX}) was investigated when TPPP (80 mg/L) was incubated with various concentrations of MMP-2 for 8 h. We chose the incubation time of 8 h since the fluorescence of TPE could reach a platform at the 8th h (Figure S6B). It was found that the fluorescence of TPE increased with MMP-2 concentration increasing, while fluorescence of PpIX was stable as an internal reference (Figure 2C). Importantly, a linear relationship was found between the F_{TPE}/F_{PpIX} ratio and concentration of MMP-2 in a certain concentration range (Figure 2D), suggesting the content of MMP-2 could be reflected by F_{TPE}/F_{PpIX} ratio. According to the crossover point among different trendlines, it was found that MMP-2 detection limit of TPPP ranged from 0.0065 mg/L to 0.303 mg/L. The wide detection range was owing to the dramatic fluorescence recovery of TPPP in the presence of MMP-2. In addition, when 0.29 mg/L MMP-2 was incubated with different concentrations of TPPP, it was found that although the fluorescences of TPE and PpIX changed with the concentration of TPPP (Figure 2E), the F_{TPE}/F_{PpIX} ratio was amazingly stable (Figure 2F), revealing the relationship between F_{TPE}/F_{PpIX} ratio and MMP-2 concentration would not be affected by the concentration change of TPPP. Obviously, this ratiometric fluorescence biosensor exhibited great advantages in accurate and quantitative determination of MMP-2 expression level. Since the retention content of traditional biosensors in tumor region was un-expectable owing to the individual difference, the enzyme triggered fluorescence signals of traditional biosensors could only demonstrate the existence of enzyme but not the detailed expression level in practical applications.[27]

Microenvironment Responsive AIE and MMP-2 Detection. The success in ratiometrical detection of MMP-2 expression encouraged us to examine whether TPPP could work in living cells. To confirm that TPPP would have contrasting fluorescence emission in response to MMP-2 changes at the cellular level, the fluorescence images were recorded by confocal laser scanning microscopy (CLSM) when 40 mg/L TPPP was incubated with SCC-7, HT1080 (HT1080 fibrosarcoma cell), HeLa (human cervix carcinoma) and COS7 (African green monkey SV40-transfected kidney fibroblast) cell-lines, respectively. These four cell-lines were chosen due to the different MMP-2 expression level. Western blotting analysis results demonstrated that the expression of MMP-2 by SCC-7 cells was the highest while healthy COS7 cells nearly had no MMP-2 expression (Figure 3H, I).[28] As expected, nearly undetectable blue signal was found in COS7 cells (Figure 3A1). On the contrary, the blue signal of TPE observably increased in tumor cell-lines in the following order: HeLa cells << HT1080 cells < SCC-7 cells (Figure 3B1-D1). Meanwhile, the red and blue signals were separated. These findings illustrated that the secreted MMP-2 by tumor cells hydrolyzed the PLGVR sequence in TPPP, leading to the detachment of TPE and PpIX. Then freed TPE initiated aggregation-induced emission. Meanwhile, higher expression of MMP-2 cleaved more TPPP, resulting in brighter blue signal. This hydrolysis process of PLGVR sequence in tumor cells was further verified by the adding of MMP-2 inhibitor, 1, 10-phenanthroline monohydrate, in SCC-7 cells. It was found that the addition of MMP-2 inhibitor decreased the blue signal dramatically (Figure 3E1), which substantially confirmed that the generation of blue signal was due to the secretion of MMP-2. Note that nearly no intensity difference was found in the red signal among different cell-lines when the TPPP was 40 mg/L, which indicated PpIX was perfect as an internal reference. Then we calculated the mean fluorescence intensity (MFI) ratio between TPE and PpIX to quantize the results of CLSM.

Encouragingly, there existed a high degree of consistency across MFI ratio (Figure 3G) and western blotting analysis (Figure 3I), Furthermore, quantitative determination of MMP-2 among these cell-lines was also conducted *via* ELISA (enzyme linked immunosorbent assay). MMP-2 expressions in COS7, HeLa, HT1080 and SCC-7 cell-lines (about 3.5×10^5 cells for each cell-line) were 0.24 ± 0.11 ng/mL, 0.77 ± 0.35 ng/mL, 2.88 ± 0.30 ng/mL and 3.69 ± 0.13 ng/mL, respectively. As expected, a similar tendency was observed between the results of quantitative MMP-2 expression and MFI ratio, which substantially indicated that the ratiometrical biosensor could accurately detect the MMP-2 expression.

To demonstrate that the MMP-2 expression level was not affected by the biosensor concentration, the concentration of biosensor was decreased to 20 mg/L. As shown in Figure 3F1-F2, although both the fluorescence intensity of PpIX and TPE decreased to some extent, the blue signal was still obvious. More importantly, the MFI_{TPE}/MFI_{PpIX} ratio had a negligible change when the concentration of biosensor decreased (Figure 3G), suggesting the MMP-2 expression level could be reflected by fluorescence ratio regardless of the concentration of biosensor. Since the expression MMP-2 was upregulated in many type of tumors, especially malignant tumors, our biosensor exhibited great potential in recognition of malignant tumors.

On-Demand Photodynamic Therapy. On the basis of the successful recognition of healthy cells from diseased ones *via* the fluorescence ratio, the feasibility of the on-demand photodynamic therapeutical efficacy was conducted *via* MTT assay. As shown in Figure 4, TPPP in COS7 cells exhibited undetectable toxicity when no light irradiation was performed. On the contrary, severe toxicity was observed regardless of cell-line difference when cells received 30 min light irradiation, suggesting the on-demand photodynamic therapy could be realized with ease *via* regulating the light irradiation condition.[29] Meanwhile, due to the improved solubility,

TPPP exhibited greater phototoxicity than free PpIX at a relative high concentration (Figure S7).

Biosensor Biodistribution, Blood Retention Time and Tumor Imaging. To confirm that TPPP could achieve MMP-2 overexpressed tumor-specific imaging *in vivo*, we established a SCC-7 tumor bearing mice model and examined *in vivo* biodistribution and tumor fluorescence imaging (Figure 5). Since PpIX has a long emission wavelengh, the fluorescence of PpIX was traced *via* small animal imaging system. It was found that this biosensor gradually accumulated in tumor tissue and reached a maximum within 6 h. Subsequently, although the fluorescence decreased with time due to the metabolism, the fluorescence was still observable even after postinjection for 24 h (Figure 5A). Meanwhile, in order to image the fluorescence in tumor and other organs, the mice were sacrificed at the 24th h. As shown in Figure 5B, although TPPP accumulated in the primary metabolic organs liver and kidney inevitably, greatest amount of TPPP appeared in tumor tissue. And the calculated MFI value revealed that the amount of biosensor in tumor tissue was even slightly higher than that in liver and kidney, and significantly higher than that in heart, spleen, lung and muscle (Figure 5C). These results were attributed to the fact that EPR effect mediated tumor selective accumulation of nano-sized biosensor could successfully trace and image the tumor tissue. To further verify that PpIX fluorescence accumulated region was the tumor tissue, two-photon small animal fluorescence imaging technique was utilized to detect the fluorescence recovery of TPE molecule (Figure 5D). As expected, bright blue fluorescence was observed in PpIX fluorescence accumulated region, indicating that the tumor biomarker MMP-2 was overexpressed in this tissue, leading to the hydrolysis of biosensor as well as the fluorescence recovery of TPE. Furthermore, fluorescence of TPE in other tissues was also observed. As shown in Figure S8, none blue signal was found in heart and the signals in spleen, lung and kidney were very weak. Although observable blue

signal was found in liver,[30] both the fluorescence intensity and area of distribution in liver were uncomparable to that in tumor region, indicating the specific MMP-2 responsibility of TPPP in tumor region. Of particular note was that EPR-induced tumor accumulation of PpIX and MMP-2-triggered AIE precisely imaged the tumor tissue, which provided an appropriate and important irradiation window for photodynamic therapy. It was also found that the accumulation of TPPP in tumor region was inseparable with the long blood retention time. As shown in Figure 5E, the concentration of TPPP in blood was still very high even up to 8 h, this relative long blood retention time was probably due to the introduction of PEG segment[31] and the formation of nanoparticles.[32]

In Vivo **Photodynamic Therapy Study.** To evaluate whether the efficient tumor accumulation of TPPP leads to enhanced therapeutic efficacy with reduced side effects, SCC-7 tumor-bearing mice were intravenously injected with TPPP solution with or without 20-min light irradiation, and PBS was used as a negative control *via* the tail vein. As shown in Figure 6A, injection of TPPP solution but without light irradiation could not inhibit the tumor growth, which was similar to the results in PBS group. However, once the mice received certain light irradiation, the growth of tumor was significantly retarded, suggesting the good antitumor efficacy of TPPP under light irradiation. Above results were also confirmed by the average tumor weight (Figure 6C) and representative tumor images (Figure 6D) at the 11th day (the mice were sacrificed at the 11th day since the tumors in control groups were too big).

In addition, the relative body weight was shown in Figure 6B, TPPP group with light irradiation had no obvious weight change, probably due to the negligible systemic toxicity of photodynamic therapy. And a series of physiological and biochemical indexes were conducted to evaluate the potential side effects in liver and kidney (Figure 6E,F).[33] It was found that there

existed negligible difference in the concentration of glutamic-pyruvate transaminase (GPT) and aspartate transaminase (AST) among PBS group and TPPP group with or without light irradiation, while the creatinine (Cr) values in all groups were too low to detect, indicating that although TPPP could appear in metabolic organs liver and kidney, low liver or kidney toxicity was observed due to none irradiation in these regions. As we know, different from the traditional chemical drugs whose undesired side effects were always accompanied by antitumor effect, the antitumor effect of photosensitizer could only be activated by light irradiation. On the other hand, ROS had a very limited action distance and short half-life period,[34] fluorescence imaging-guided precise photodynamic therapy could restrict ROS and phototoxicity in the tumor region furthest, which significantly decreased side effect. The well photodynamic therapy with low systemic toxicity was also demonstrated by Hematoxylin & Eosin (H&E) staining (Figure 6G). Clearly, very few cells were dead in the tumor tissue of TPPP group without light irradiation. In contrast, a large amount of cells were dead in the tumor tissue of TPPP group with light irradiation while undetectable physiological morphology changes were found in heart, liver, spleen, lung, kidney and muscle tissues.

CONCLUSIONS

In summary, a tumor microenvironment responsive ratiometric biosensor TPPP was developed to realize tumor imaging and precise photodynamic antitumor therapy. This ratiometric biosensor successfully differentiated the expression level of MMP-2 among different cell-lines regardless of the biosensor concentration according to the fluorescence intensity ratio between TPE and PpIX. Importantly, nano-sized TPPP could effectively accumulate in tumor region *via* EPR effect, MMP-2 responsive dual-fluorescence imaging of both TPE and PpIX pointed out the tumor tissue accurately, which guided the precise photodynamic therapy in the tumor tissue,

realizing enhanced therapeutical efficacy with minimal side effects. This strategy opens a window for designing of ratiometric biosensor in tumor imaging and"precision medicine", which will have great potential in practical treatment.

MATERIALS AND METHODS

Materials. Detailed material information was provided in our previous article.[35] Additionally, PpIX was obtained from Aladdin-Reagent Co. Ltd. (China). DCFH-DA was provided by Beyotime Institute of Biotechnology (China). Fmoc-PEG_8-COOH was provided by Zhoubei Technology Co. Ltd. (Hangzhou, China).

TPE-COOH Synthesis. TPE-COOH was synthesized as previous report.[36] Briefly, Under N_2 atmosphere, 4-hydroxybenzophenone (9.5g, 0.05 mol), benzophenone (9.1g, 0.05 mol) and zinc powder (8 g, 0.12 mmol) were mixed with 200 mL tetrahydrofuran (THF) at 0 °C. Then, $TiCl_4$ (6.5 mL, 0.06 mmol) was added under 10 °C. The mixture was stirred at the room temperature for 0.5 h followed by reflux overnight. After the mixture was cooled to room temperature, 25 mL hydrochloric acid (1 mmol/L) was added and extracted with dichloromethane (DCM). The crude product was purified by a silica gel column (DCM : petroleum ether = 3 : 1) and TPE-OH was obtained. Subsequently, TPE-OH (1.75 g, 5 mmol), tert-Butylbromoacetate (1 g, 5mmol) and K_2CO_3 (1 g, 7.5 mmol) were mixed with 25 mL acetonitrile. The mixture was reflux overnight. The solution was separated by filtration. The crude product was purified through silica gel column. This product was added into a solution (DCM : TFA = 1 : 1) and stirred vigorously for 1.5 h. The solution was poured into DI water and extracted with DCM. The organic layer was concentrated. TPE-COOH was obtained by repeatedly dissolution and precipitation to remove the trifluoroacetic acid (TFA). TPE-COOH was characterized by electrospray ionization mass

spectrometry (ESI-MS) system (Finnigan LCQadvantage) and Nuclear magnetic resonance spectroscopy (^{1}H NMR, d_6, DMSO).

TPPP Synthesis. TPPP (TPE-PLGVR$_2$-(PEG$_8$)$_2$-K(PpIX)) was synthesized as our previous report.[22] The TPPP was loaded on a rink amide resin (0.51 mmol/g). The amino acid couplings were conducted with Fmoc-protected amino acid, HBTU and diisopropylethylamine for 2.5 h. During the synthesis, Kaiser reagent was empolyed to test the coupling efficacy, and 20% piperdine/DMF (v/v) was used to cleave the Fmoc protecting group for two times (10 min + 10 min). After TPE was coupled, the Mtt protecting group was selectively moved with 1% TFA in DCM 9 × 5 min. The resin was repeatedly washed with DMF, then PpIX was conjugated to the lateral chain of Lys. Subsequently, TPPP was cleaved from resin in a cleavage cocktail of TFA, triisopropylsilane (TIS) and H_2O in the volume ratio of 95: 2.5: 2.5 for 1.5 h. The product was precipitated in cold ether and collected. TPPP was then dried in vacuum. TPPP was charaterized *via* ESI-MS and ^{1}H NMR (d_6, DMSO, Figure S3B).

Cell Culture. SCC-7, HT1080, HeLa and COS7 cells were incubated in DMEM medium at 37°C with a 5% CO_2 atmosphere. The DMEM medium contained 10% heat-inactivated FBS as well as 1% antibiotics (penicillin-streptomycin, 10000 U /mL).

TEM Observation. Morphology of TPPP (80 mg/L) was observed by TEM (JEM-2100 microscope). Before observation, TPPP was stained with phosphotungstic acid solution.

Singlet Oxygen Detection. The generation of $^1O_2$ was determined by fluorescence spectrum as well as CLSM (for intracellular ROS) using DCFH-DA as the sensor. For fluorescence spectrum, DCFH-DA was pretreated with NaOH and then mixed with TPPP (40 mg/L). The fluorescence spectra were recorded at preset times with an excitation wavelength of 488 nm. PpIX (8.6 mg/L

in 2.5% DMSO) were used as a negative control. For CLSM observation, SCC-7 cells were incubated with various samples for 4 h. And then the medium was replaced. DCFH-DA was added (final concentration 10 μM) and the cells were incubated for 20 min. Light irradiation was performed subsequently (band pass: 400-700 nm, 3.3 mW/cm^2). The cells were repeatedly washed and then observed as soon as possible *via* CLSM (Ex = 488 nm, Em = band pass 500-550 nm).

MMP-2 Enzymatic Response of TPPP. The MMP-2 enzymatic response of AIE fluorescence recovery was investigated by fluorescence spectra at 37 °C. The excitation wavelength of AIE was 330 nm. Briefly, 80 mg/L TPPP was incubated in the presence or absence of 0.40 mg/mL of MMP-2 (pH 7.4, 10 mM PBS). The fluorescence spectra were recorded at preset times on a LS55 luminescence spectrometer (Perkin-Elmer). To test the detection sensitivity, 80 mg/L TPPP solution was incubated with various concentrations of MMP-2 and the fluorescence spectrums at 1 min were recorded. The fluorescence intensity ratios between TPE and PpIX at the 8th h with different concentrations of TPPP or MMP-2 were also determined. The excitation wavelength of PpIX was 409 nm, while the excitation wavelength of TPE was 330 nm.

MMP-2 Detection *via* CLSM. The MMP-2 expression difference among different cell-lines was measured *via* CLSM. SCC-7, HT1080, HeLa and COS7 were chosen as the experiment cell models. Briefly, cells (1×10^5 cells/well) were seeded on a 6-well plate. After 24 h, preset amount of TPPP solution was added. The cells were imaged directly *via* CLSM after incubated for 8 h. The fluorescence images were determined with a filter set (Ex = 405 nm, Em = band pass 450-500 nm) for TPE and a filter set (Ex = 488 nm, Em = band pass 600-700 nm) for PpIX. Additionally, to determine the MMP-2 expression, the MMP-2 inhibitor was added 2 h early

before TPPP was added. The mean fluorescence intensity of TPE and PpIX was measured by Image J software.

Cytotoxicity Assay *In Vitro*. The cytotoxicity of TPPP against SCC-7 and COS7 cells *in vitro* was tested *via* MTT assay. Cells were seeded on a 96-well plate at a density of 6000 cells/well and incubated for 24 h. Then TPPP at various concentrations was added to each well. After 6 h, the cells received 0 min or 30 min light irradiation (3.3 mW/cm^2, 400-700 nm). Cells were incubated for 48 h and then the medium was replaced with 200 μL fresh medium. 20 μL MTT was added to each well. 4 h later, the medium was replaced with 200 μL DMSO. The absorbance at 570 nm was measured by a microplate reader (Bio-Rad, Model 550, USA). Cell viability was defined as the percentage of survival cells per total nontreated cells. All data were averaged from eight independent experiments.

***In Vivo* Optical Imaging, Tissue Distributions, and Pharmacokinetics.** The animal experiments were conducted according to the guidelines for laboratory animals established by the Wuhan University Center for Animal Center Experiment/A3-Lab. SCC-7 tumor model was developed by subcutaneous injection of 1×10^6 cells per mouse. SCC-7 tumor-bearing mice were intravenously injected with 200 μL TPPP solution *via* tail vein (18.5 mg/kg per mouse). At the preset time after injection of TPPP solution, mice were anesthetized and imaged *via* small animal imaging system. 630 nm was used as the excitation wavelength, while long wave fluorescence emission signal (600–700 nm) was collected. For two-photon excited fluorescence imaging study, the tumor and other tissues were observed by CLSM at the 6th h after postinjection, the excitation wavelength was 720 nm and fluorescence emission signal (420–500 nm) was collected. For tissue distribution study, mice were sacrificed at the 48th h after injection. The tissues including muscle, heart, liver, spleen, lung, kidney, and tumor were collected and imaged. For

pharmacokinetic study, mice were injected with TPPP (18.5 mg/kg per mouse) *via* tail vein. The blood samples were obtained at the 0.5, 1, 2, 4, 6, 8, 10 and 24 h time points. Appropriate PBS was added. The samples were repeatedly freeze-thawed, and then ultrasonication for 5 min. The samples were centrifuged at 3000 r/min for 4 min. The fluorescence of supernate was determined by fluorescence spectroscopy, while the standard curve was determined *via* fluorescence spectrum (Ex = 409 and Ex = 630 nm).

***In Vivo* Systemic Toxicity.** At the 11th day, the blood was extracted from different mice groups. After the blood samples were solidified, the samples were centrifuged at 3000 r/min for 5 min. The serum was collected. The contents of glutamic-pyruvate transaminase, aspartate transaminase and creatinine were detected at Wuhan Xiehe Hospital.

***In Vivo* Antitumor Study.** Mice were injected with 100 μL SCC-7 cells (1×10^6 cells per mouse). When the tumors reached an approximate size of 100 mm^3, the mice were divided into three groups randomly. Each group had 6 mice. The mice were injected with 200 μL PBS buffer and TPPP (two groups) at the preset day, respectively. After injected for 8 h, one TPPP group received 20-min light irradiation (630 nm, 220 mW/cm^2), the other TPPP group received none light irradiation. The dose of PpIX was 4 mg/kg per mouse. The tumor size and mice weight were measured every day. The tumor volume was defined as: V = ((tumor length) × (tumor width)^2)/2. Relative tumor volume was calculated as V/V_0 (V_0 was the tumor volume when the treatment was initiated). Relative body weight was defined as M/M_0 (M_0 was the body weight of mouse when the treatment was initiated). When the mice were sacrificed, the muscle, heart, liver, spleen, lung, kidney, and tumor tissue were collected for further histological examinations *via* H&E staining.

Statistical Analysis. Statistical analysis was performed using a Student's t-test. The differences were considered to be statistical significant for p value < 0.05.

ASSOCIATED CONTENT

Supporting Information. Synthetic process of TPPP, ESI-MS spectrum and ^{1}H NMR, TEM image, ROS generation study, fluorescence spectrum of TPPP, cell viability of PpIX against COS7 cells, Two-photon imaging of heart, liver, spleen, lung and kidney. This material is available free of charge *via* the Internet at http://pubs.acs.org.

Corresponding Author

*Corresponding Author: xz-zhang@whu.edu.cn

Author Contributions

K. H., X. Z. wrote the paper. †These authors contributed equally.

Notes

The authors declare no competing financial interest.

ACKNOWLEDGMENT

This work was supported by the National Natural Science Foundation of China (51125014, 51233003 and 21474077) and the Ministry of Science and Technology of China (2011CB606202).

REFERENCES

1. Idris, N. M.; Gnanasammandhan, M. K.; Zhang, J.; Ho, P. C.; Mahendran, R.; Zhang, Y. *In Vivo* Photodynamic Therapy Using Upconversion Nanoparticles as Remote-Controlled Nanotransducers. *Nat. Med.* **2012**, *18*, 1580–1585.

2. Brown, S. Photodynamic Therapy: Two Photons Are Better Than One. *Nat. Photon*. **2008**, *2*, 394–395.

3. Zhang, T.; Lan, R. F.; Chan, C. F.; Law, G. L.; Wong, W. K.; Wong, K. L. *In Vivo* Selective Cancer-Tracking Gadolinium Eradicator as New-Generation Photodynamic Therapy Agent. *Proc. Natl. Acad. Sci. U. S. A.* **2014**, *111*, 5492–5497.

4. Sanabria, L. M.; Rodríguez, M. E.; Cogno, I. S.; Vittar, N. B. R.; Pansa, M. F.; Lamberti, M.; Rivarola, V. A. Direct and Indirect Photodynamic Therapy Effects on the Cellular and Molecular Components of the Tumor Microenvironment. *BBA-Rev. Cancer* **2013**, *1835*, 36–45.

5. Pan, L. M.; Liu, J. N.; Shi, J. L. Intranuclear Photosensitizer Delivery and Photosensitization for Enhanced Photodynamic Therapy with Ultralow Irradiance. *Adv. Funct. Mater.* **2014**, *24*, 7318–7327.

6. Cheng, Y.; Morshed, R. A.; Auffinger, B.; Tobias, A. L.; Lesniak, M. S. Multifunctional Nanoparticles for Brain Tumor Imaging and Therapy. *Adv. Drug Deliver. Rev.* **2014**, *66*, 42–57.

7. Ethirajan, M.; Chen, Y. H.; Joshi, P.; Pandey, R. K. The Role of Porphyrin Chemistry in Tumor Imaging and Photodynamic Therapy. *Chem. Soc. Rev.* **2011**, *40*, 340–362.

8. Lindner, U.; Trachtenberg, J.; Lawrentschuk, N. Focal Therapy in Prostate Cancer: Modalities, Findings and Future Considerations. *Nat. Rev. Urology* **2010**, *7*, 562–571.

9. Chen, D. Q.; Wang, C.; Nie, X.; Li, S. M.; Li, R. M.; Guan, M. R.; Liu, Z.; Chen, C. Y.; Wang, C. R.; Wan, L. J.; *et al.* Photoacoustic Imaging Guided Near-Infrared Photothermal Therapy Using Highly Water-Dispersible Single-Walled Carbon Nanohorns as Theranostic Agents. *Adv. Funct. Mater.* **2014**, *24*, 6621–6628.

10. Zheng, G.; Chen, J.; Stefflova, K.; Jarvi, M.; Li, H.; Wilson, B. C. Photodynamic Molecular Beacon as an Activatable Photosensitizer Based on Protease-Controlled Singlet Oxygen Quenching and Activation. *Proc. Natl. Acad. Sci. U. S. A.* **2007**, *104*, 8989–8994.

11. Wüstner, D.; Solanko, L. M.; Lund, F. W.; Sage, D.; Schroll, H. J.; Lomholt, M. A. Quantitative Fluorescence Loss in Photobleaching for Analysis of Protein Transport and Aggregation. *BMC Bioinformatics* **2012**, *13*, 296–317.

12. Chen, Y. C.; Zhu, C. C.; Yang, Z. H.; Chen, J. J.; He, Y. F.; Jiao, Y.; He, W. J.; Qiu, L.; Cen, J. J.; Guo, Z. J. A Ratiometric Fluorescent Probe for Rapid Detection of Hydrogen Sulfide in Mitochondria. *Angew. Chem.* **2013**, *125*, 1732 –1735.

13. Myochin, T.; Kiyose, K.; Hanaoka, K.; Kojima, H.; Terai, T.; Nagano, T. Rational Design of Ratiometric Near-Infrared Fluorescent pH Probes with Various pKa Values, Based on Aminocyanine. *J. Am. Chem. Soc.* **2011**, *133*, 3401–3409.

14. Tsai, Y. T.; Zhou, J.; Weng, H.; Shen, J. H.; Tang, L. P.; Hu, W. J. Real-Time Noninvasive Monitoring of *in Vivo* Inflammatory Responses Using a pH Ratiometric Fluorescence Imaging Probe. *Adv. Healthcare Mater.* **2014**, *3*, 221–229.

15. Albers, A. E.; Okreglak, V. S.; Chang, C. J. A FRET-Based Approach to Ratiometric Fluorescence Detection of Hydrogen Peroxide. *J. Am. Chem. Soc.* **2006**, *128*, 9640–9641.

16. Shi, P.; Liu, Z.; Dong, K.; Ju, E. G.; Ren, J. S.; Du, Y. D.; Li, Z. Q.; Qu, X. G. A Smart "Sense-Act-Treat" System: Combining a Ratiometric pH Sensor with a Near Infrared Therapeutic Gold Nanocage. *Adv. Mater.* **2014**, *26*, 6635–6641.

17. Tian, J. W.; Ding, L.; Ju, H. X.; Yang, Y. C.; Li, X. L.; Shen, Z.; Zhu, Z.; Yu, J. S.; Yang, C. Y. J. A Multifunctional Nanomicelle for Real-Time Targeted Imaging and Precise Near-Infrared Cancer Therapy. *Angew. Chem., Int. Ed.* **2014**, *53*, 9544–9549.

18. Savariar, E. N.; Felsen, C. N.; Nashi, N.; Jiang, T.; Ellies, L. G.; Steinbach, P.; Tsien, R. Y.; Nguyen, Q. T. Real-Time *in Vivo* Molecular Detection of Primary Tumors and Metastases with Ratiometric Activatable Cell-Penetrating Peptides. *Cancer Res.* **2013**, *73*, 855–864.

19. Leung, C. W. T.; Hong, Y. N.; Chen, S. J.; Zhao, E. G.; Lam, J. W. Y.; Tang, B. Z. A Photostable AIE Luminogen for Specific Mitochondrial Imaging and Tracking. *J. Am. Chem. Soc.* **2013**, *135*, 62–65.

20. Ding, D.; Li, K.; Liu, B.; Tang, B. Z. Bioprobes Based on AIE Fluorogens. *Acc. Chem. Res.* **2013**, *46*, 2441–2453.

21. Rananaware, A.; Bhosale, R. S.; Patil, H.; Kobaisi, M. A.; Abraham, A.; Shukla, R.; Bhosale, S. V.; Bhosale, S. V. Precise Aggregation-Induced Emission Enhancement *via* H^+ Sensing and Its Use in Ratiometric Detection of Intracellular pH Values. *RSC Adv.* **2014**, *4*, 59078–59082.

22. Chen, C. S.; Xu, X. D.; Wang, Y.; Yang, J.; Jia, H. Z.; Cheng, H.; Chu, C. C.; Zhuo, R. X.; Zhang, X. Z. A Peptide Nanofibrous Indicator for Eye-Detectable Cancer Cell Identification. *Small* **2013**, *9*, 920–926.

23. Cabral, H.; Matsumoto, Y.; Mizuno, K.; Chen, Q.; Murakami, M.; Kimura, M.; Terada, Y.; Kano, M. R.; Miyazono, K.; Kataoka, K.; *et al.* Accumulation of Sub-100 nm Polymeric Micelles in Poorly Permeable Tumours Depends on Size. *Nat. Nanotechnol.* **2011**, *6*, 815–823.

24. Ding, H. Y.; Sumer, B. D.; Kessinger, C. W.; Dong, Y.; Huang, G.; Boothman, D. A.; Gao, J. M. Nanoscopic Micelle Delivery Improves the Photophysical Properties and Efficacy of Photodynamic Therapy of Protoporphyrin IX. *J. Controlled Release* **2011**, *151*, 271–277.

25. Han, K.; Lei, Q.; Wang, S. B.; Hu, J. J.; Qiu, W. X.; Zhu, J. Y.; Yin, W. N.; Luo, X.; Zhang, X. Z. Dual-Stage-Light-Guided Tumor Inhibition by Mitochondria-Targeted Photodynamic Therapy. *Adv. Funct. Mater.* **2015**, *25*, 2961–2971.

26. Shi, H. B.; Kwok, R. T. K.; Liu, J. Z.; Xing, B. G.; Tang, B. Z.; Liu, B. Real-Time Monitoring of Cell Apoptosis and Drug Screening Using Fluorescent Light-up Probe with Aggregation-Induced Emission Characteristics. *J. Am. Chem. Soc.* **2012**, *134*, 17972−17981.

27. Chang, C. J.; Jaworski, J.; Nolan, E. M.; Sheng, M.; Lippard, S. J. A Tautomeric Zinc Sensor for Ratiometric Fluorescence Imaging: Application to Nitric Oxide-Induced Release of Intracellular Zinc. *Proc. Natl. Acad. Sci. U. S. A.* **2003**, *101*, 1129–1134.

28. Lee, S.; Cha, E. J.; Park, K.; Lee, S. Y.; Hong, J. K.; Sun, I. C.; Kim, S. Y.; Choi, K.; Kwon, I. C.; Ahn, C. H.; *et al.* A Near-Infrared-Fluorescence-Quenched Gold-Nanoparticle Imaging

Probe for *in Vivo* Drug Screening and Protease Activity Determination. *Angew. Chem.* **2008**, *120*, 2846 –2849.

29. Wang, B.; Yuan, H. X.; Liu, Z.; Nie, C. Y.; Liu, L. B.; Lv, F. T.; Wang, Y. L.; Wang, S. Cationic Oligo (p-Phenylene Vinylene) Materials for Combating Drug Resistance of Cancer Cells by Light Manipulation. *Adv. Mater.* **2014**, *26*, 5986–5990.

30. Akers, W. J.; Xu, B. G.; Lee, H.; Sudlow, G. P.; Fields, G. B.; Achilefu, S.; Edwards, W. B. Detection of MMP-2 and MMP-9 Activity *in Vivo* with a Triple-Helical Peptide Optical Probe. *Bioconjugate Chem.* **2012**, *23*, 656−663.

31. Gref, R.; Domb, A.; Quellec, P.; Blunk, T.; Müller, R. H.; Verbavatz, J. M.; Langer, R. The Controlled Intravenous Delivery of Drugs Using PEG-Coated Sterically Stabilized Nanospheres. *Adv. Drug Deliver. Rev.* **2012**, *64*, 316–326.

32. Huang, P.; Wang, D. L.; Su, Y.; Huang, W.; Zhou, Y. F.; Cui, D. X.; Zhu, X. Y.; Yan, D. Y. Combination of Small Molecule Prodrug and Nanodrug Delivery: Amphiphilic Drug-Drug Conjugate for Cancer Therapy. *J. Am. Chem. Soc.* **2014**, *136*, 11748−11756.

33. Tang K.; Zhang Y.; Zhang H. F.; Xu, P. W.; Liu, J.; Ma, J. W.; Lv, M.; Li, D. P.; Katirai, F.; Huang, B.; *et al.* Delivery of Chemotherapeutic Drugs in Tumour Cell-Derived Microparticles. *Nat. Commun.* **2012**, *3*, 1282–1293.

34. Han, K.; Lei, Q.; Jia, H. Z.; Wang, S. B.; Yin, W. N.; Chen, W. H.; Cheng, S. X.; Zhang, X. Z. A Tumor Targeted Chimeric Peptide for Synergistic Endosomal Escape and Therapy by Dual-Stage Light Manipulation. *Adv. Funct. Mater.* **2015**, *25*, 1248–1257.

35. Han, K.; Liu, Y.; Yin, W. N.; Wang, S. B.; Xu, Q.; Zhuo, R. X.; Zhang, X. Z. A FRET-Based Dual-Targeting Theranostic Chimeric Peptide for Tumor Therapy and Real-Time Apoptosis Imaging. *Adv. Healthcare Mater.* **2014**, *3*, 1765–1768.

36. Wang, H. B.; Huang, Y.; Zhao, X. P.; Gong, W.; Wang, Y.; Cheng, Y. Y. A Novel Aggregation-Induced Emission Based Fluorescent Probe for an Angiotensin Converting Enzyme (ACE) Assay and Inhibitor Screening. *Chem. Commun.* **2014**, *50*, 15075–15078.

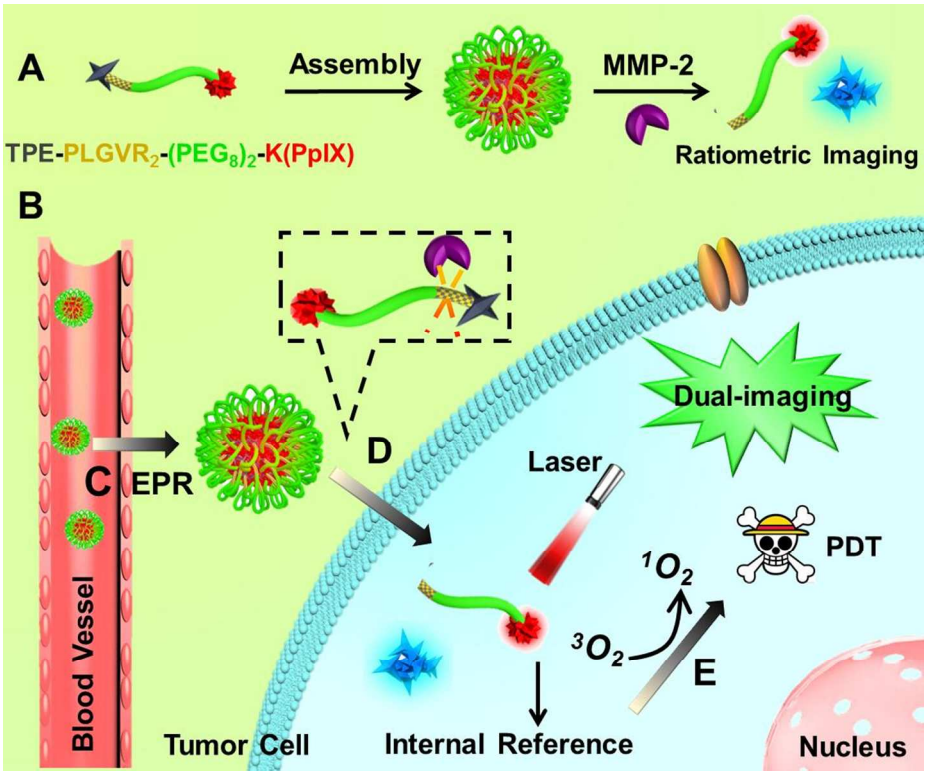

Scheme 1. (A) Self-assembly of TPPP into nanoparticles; (B) the intravenously injection of TPPP into mice *via* vein injection; (C) accumulation of TPPP in tumor region *via* EPR; (D) the hydrolysis of TPPP and the fluorescence recovery of TPE; (E) AIE-guided photodynamic antitumor therapy.

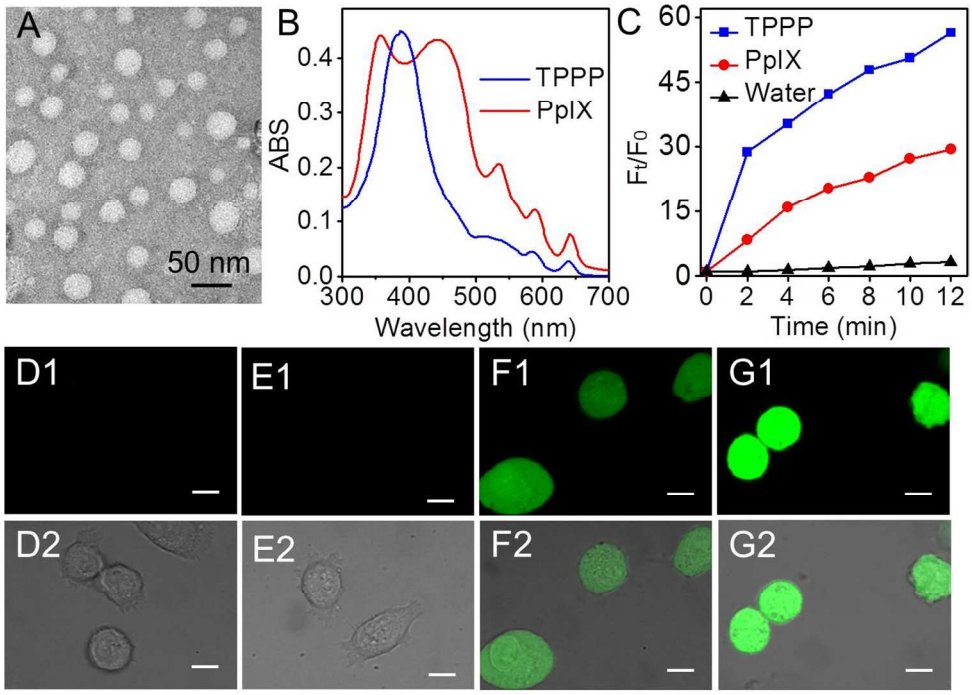

Figure 1. (A) TEM image and (B) UV-vis spectrum of TPPP. (C) ROS production of TPPP with different irradiation times that was measured by fluorescence spectrum. Water and free PpIX (in 2.5% DMSO) were used as negative controls. Intracellular ROS formation mediated by various samples: (D1-D2) blank control; (E1-E2) TPE (6.2 mg/L in 2.5% DMSO); (F1-F2) free PpIX (8.6 mg/L in 2.5% DMSO); (G1-G2) TPPP (40 mg/L). The irradiation time was 20 min, and the scale bar was 10 μm. The excitation wavelength of DCF was 488 nm. D1-G1: DCF fluorescence (green) depicted intracellular ROS; D2-G2: overlay images.

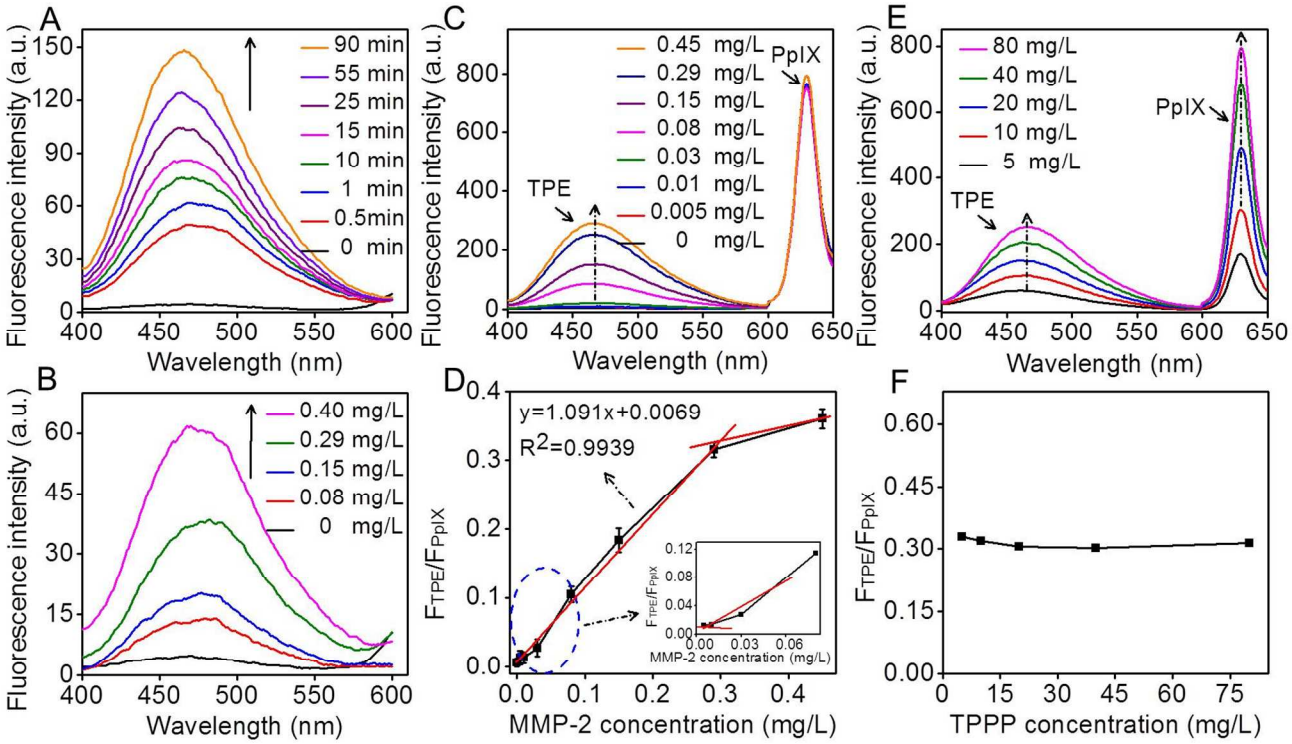

Figure 2. Fluorescence recovery of TPE when TPPP (80 mg/L) was incubated with (A) 0.4 mg/L MMP-2 for different times and (B) various concentrations of MMP-2 for 1 min. (C) The fluorescence spectrum of TPE and PpIX and (D) the fluorescence intensity ratios when TPPP (80 mg/L) was incubated with various concentrations of MMP-2 for 8 h. (E) The fluorescence spectrum of TPE and PpIX and (F) the fluorescence intensity ratios when TPPP at different concentrations were incubated with 0.29 mg/L MMP-2 for 8 h. The excitation wavelengths of PpIX and TPE were 409 nm and 330 nm, respectively.

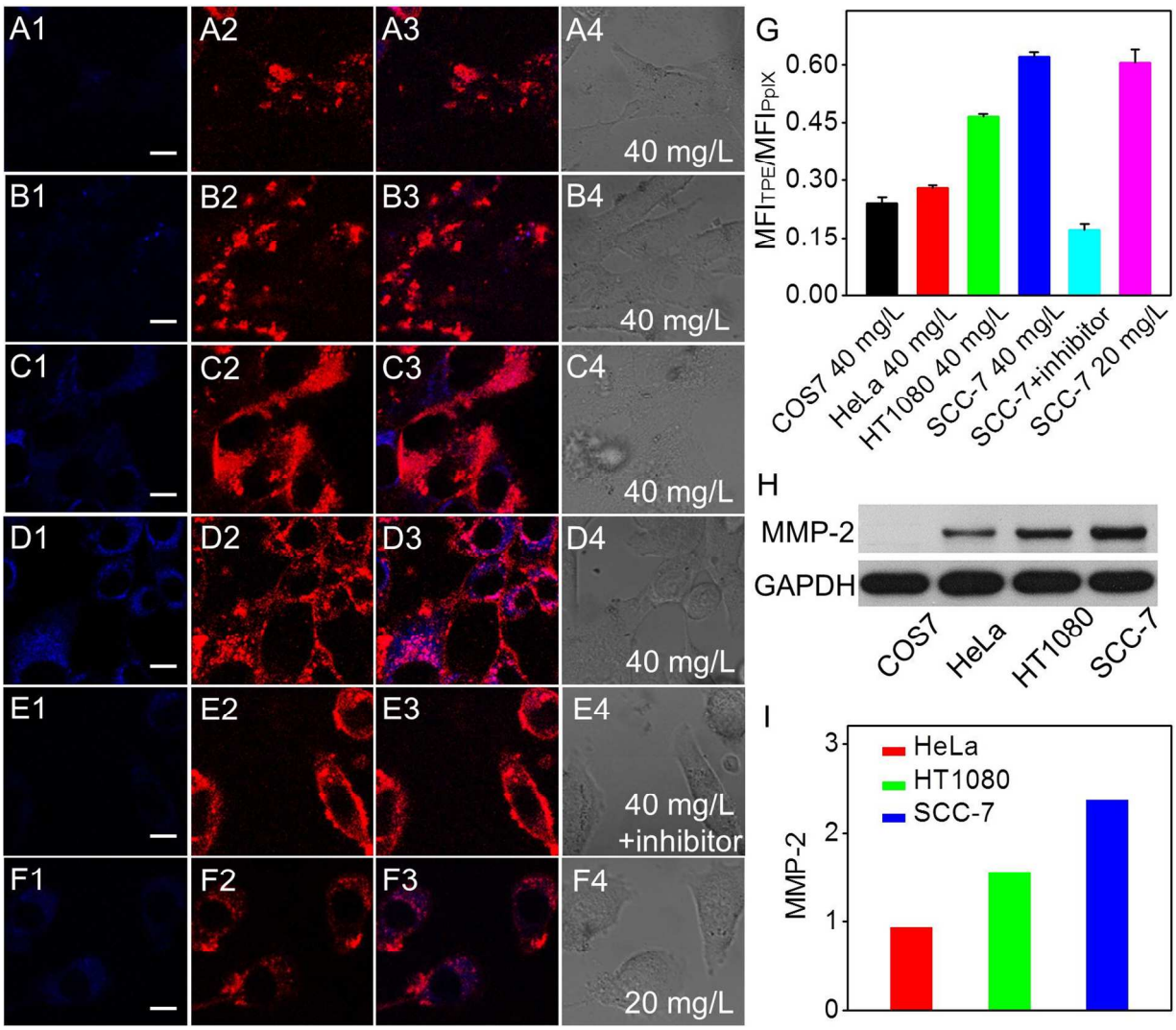

Figure 3. The fluorescence recovery of TPE when 40 mg/L TPPP was incubated with (A) COS7 cells, (B) HeLa cells, (C) HT1080 cells, (D) SCC-7 cells. (E) 40 mg/L TPPP was incubated with SCC-7 cells with MMP-2 inhibitor. (F) 20 mg/L TPPP was incubated with SCC-7 cells. The excitation wavelengths of PpIX and TPE were 488 nm and 405 nm, respectively. Blue signal: TPE; Red signal: PpIX; A4-F4: bright field. The scale bar was 10 μm. (G) MFI_{TPE}/MFI_{PpIX} values were calculated by image J. (H) Western blotting analysis of MMP-2 among different cell-lines and (I) the gray values.

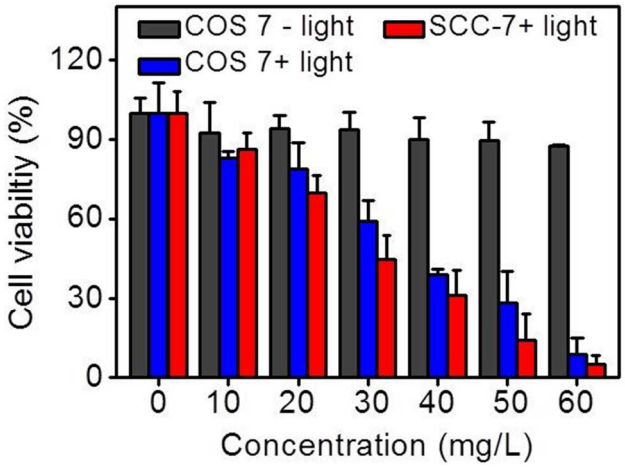

Figure 4. Cytotoxicity of TPPP against SCC-7 cells (with 30 min light irradiation) and COS7 cells (with 30 min or without light irradiation).

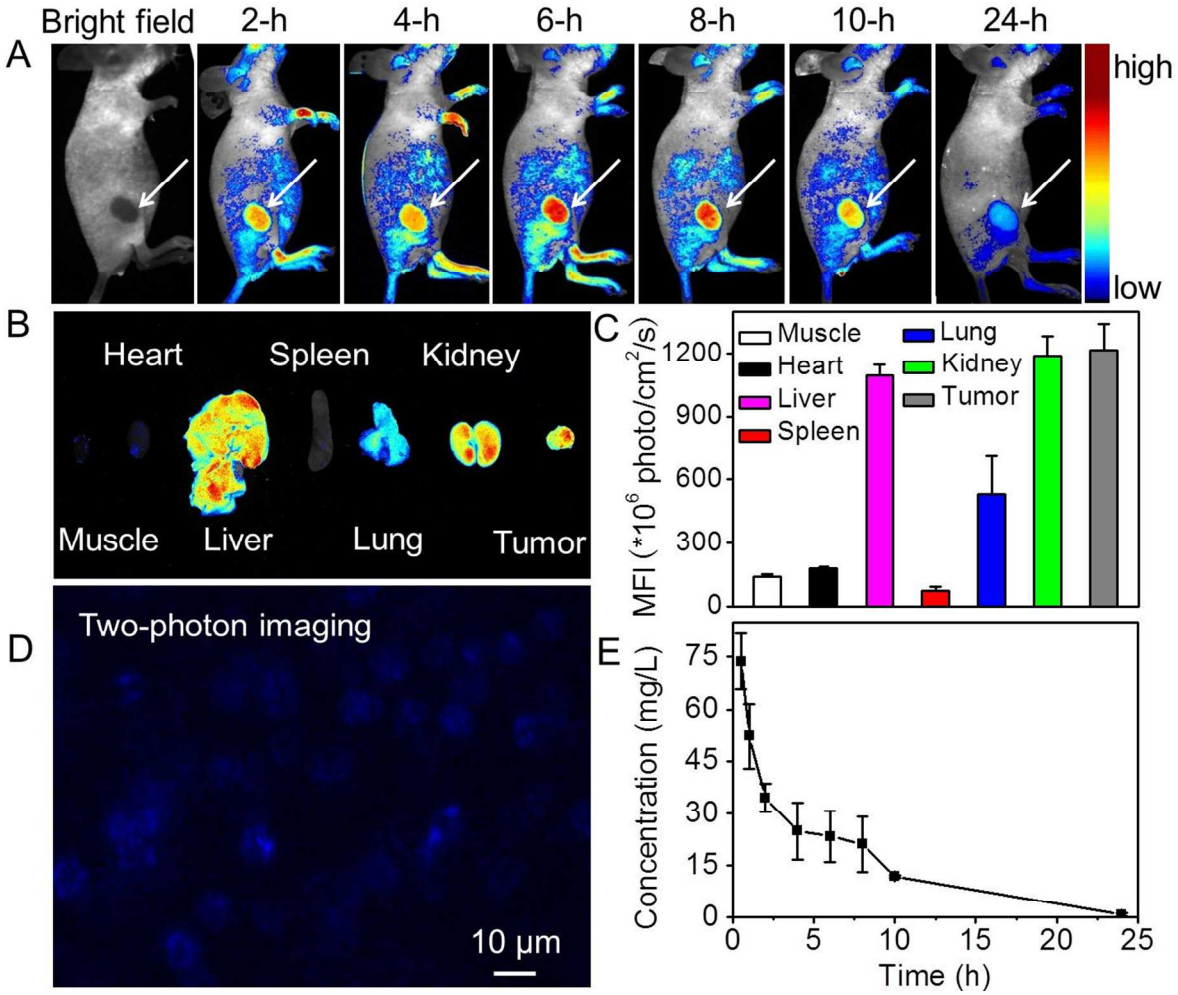

Figure 5. (A) Biodistribution imagings of SCC-7 tumor-bearing mice after intravenous injection of TPPP, the white arrow pointed at tumor tissue. The excitation wavelength of PpIX was 630 nm. (B) Tissue imaging and (C) the corresponding MFI values at the 24th h after postinjection. (D) Two-photon imaging of the tumor tissue while the excitation wavelength was 720 nm for TPE. (E) Blood retention kinetic of TPPP (at 4 mg PpIX equiv. kg^{-1}) after intravenous injection.

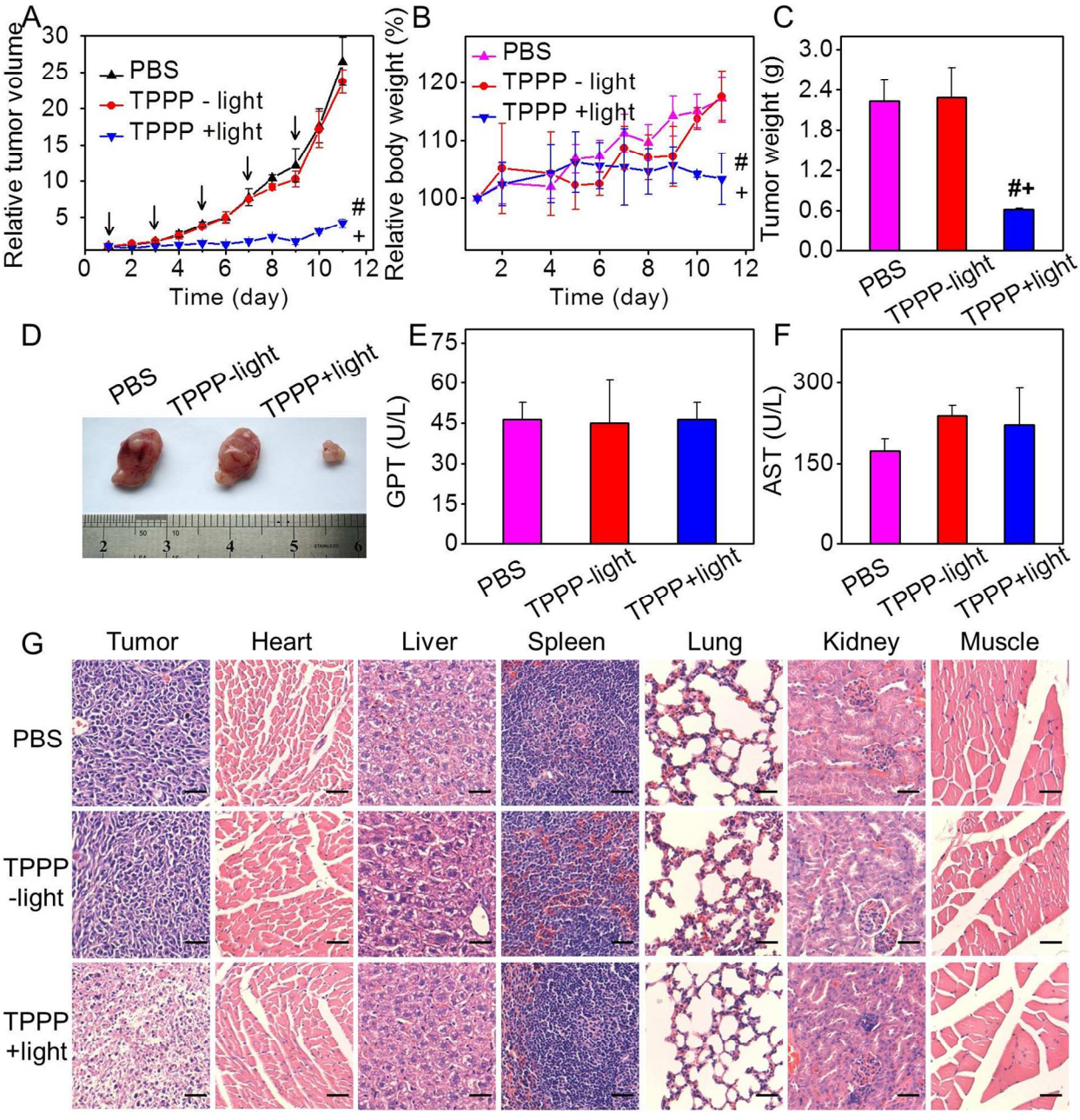

Figure 6. Antitumor study *in vivo via* intravenous injection. (A) Relative tumor volume after post-treatment, the arrow represented the injection of TPPP solution; (B) relative body weight; (C) average tumor weight and (D) representative tumor images at the 11th day. (E) Serum levels of glutamic-pyruvate transaminase and (F) aspartate transaminase were detected. Every group

had 6 mice, $^{\#}p < 0.05$ and $^{+}p < 0.05$ were determined by a Student's t-test when the group was compared with the groups that treated with PBS and TPPP without light irradiation, respectively. (G) H&E staining of tumor tissues and other tissues. The scale bar was 50 μm.

TOC Graphic

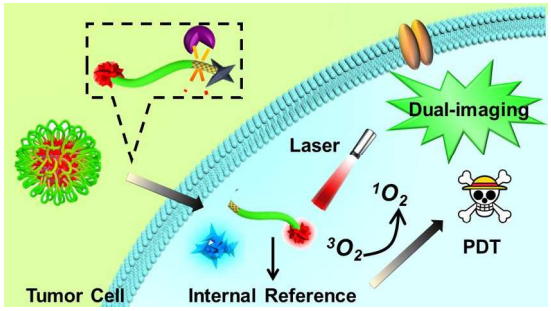
Dual-imaging
Laser
$^1O_2$
$^3O_2$
PDT
Tumor Cell
Internal Reference